Mechanical Design Considerations of an "Ironless," High-Specific-Power Electric Machine

Yuanshan Chen, *Member, IEEE*, Reed Sanchez, *Member, IEEE*, Andy Yoon, *Student Member, IEEE*, and Kiruba Sivasubramaniam Haran, *Fellow, IEEE*

***Abstract*— This paper describes the mechanical design considerations for a 1 MW, 14 000 rpm motor which achieves a specific power of at least 13 kW/kg. This is enabled through an "ironless," inside out, Halbach array permanent magnet, high frequency, and airgap or slotless configuration. The "ironless" design creates mechanical challenges because thin radial builds which reduce weight also typically reduce structural stability and vibrational damping. Structural deformation challenges include radial expansion and static bending. Vibrational issues include stator resonance mode excitation as well as rotor dynamic resonance excitation. The mechanical challenges were studied with analytical calculations and high-fidelity finite-element analysis. These analyses drove design refinements to mitigate these challenges. The rotor has then been tested to verify these analysis results.**

***Index Terms*— Aircraft power systems, permanent magnet motors, rotating machine mechanical factors, traction motors.**

I. Introduction

NASA has identified the achievement of 13-kW/kg specific power for megawatt class electric motors as a key milestone for the development of future hybrid-electric aircraft [1]. This has driven machine designers toward options that use limited amounts of ferromagnetic steel, which traditionally helps to carry magnetic flux, enhances the structural integrity of machines both on the rotor and the stator, and helps minimize dynamic modes. Mechanical performance, both static and dynamic, becomes crucial to obtain a robust design. This paper discusses the key mechanical design aspects for the megawatt scale high-frequency motor design initially presented in [2].

The proposed motor is shown in Fig. 1. The dimensions and operating point have been optimized since [2]. Analysis indicates that the machine will produce 1 MW of output power but weigh only about 70 kg, resulting in a power density of 14.1 kW/kg, which makes it very attractive compared to the state of the art [3]. Key parameters are summarized in Table I.

To achieve 1 MW of power at reduced motor weight, the proposed motor is designed to operate at high speed (14 000 rpm). Thus, an outer rotor topology is selected to allow sufficient retaining ring thickness without increasing the air-gap length and degrading electromagnetic performance. The retaining ring also allows for a high tip speed, which is crucial to high power density. To reduce the radial dimension of the stator yoke, which reduces machine weight, a high number of poles, 10 pole pairs, is adopted. To further reduce the weight of the machine, the rotor yoke is eliminated by employing Halbach arrays, which allow cancellation, on the order of mT, of magnetic field on the outside while maintaining an air-gap field of approximately 0.9 T. An airgap or slotless winding topology eliminates stator teeth and enables high-frequency operation with Litz wire conductors [4].

The main mechanical design challenges for this high power density design are structural deformation and vibration. Section II describes the structural deformation. Section III describes the vibrational analysis on both static and rotating components. Section IV describes the experimental results validating the structural deformation and vibration analyses.

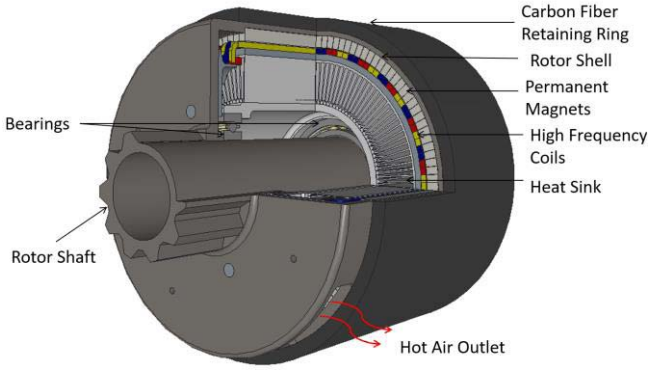

Fig. 1. Proposed machine for Aircraft Turbo-Electric Propulsion.

TABLE I
Proposed Motor Key Performance Ratings

Power Density	14.1 kW/kg
Efficiency	98.6%
Number of Poles	20
Rated Speed	14000 rpm
Output Power	1 MW
Weight	70.6 kg
Frequency	2333 Hz
Tip Speed	242 m/s

II. Design for Structural Deformation

The structural challenges presented here include radial expansion of the rotor due to high speed and deflection of the

Manuscript received October 31, 2016; revised April 1, 2017 and May 29, 2017; accepted July 18, 2017. Date of publication July 31, 2017; date of current version December 4, 2017. This work was supported by NASA Fixed Wing Research under Grant NNX14AL79A. *(Corresponding author: Reed Sanchez.)*

The authors are with the Department of Electrical and Computer Engineering, University of Illinois at Urbana–Champaign, Champaign, IL 61801 USA (e-mail: reedsanch@gmail.com.)

Digital Object Identifier 10.1109/TTE.2017.2733763

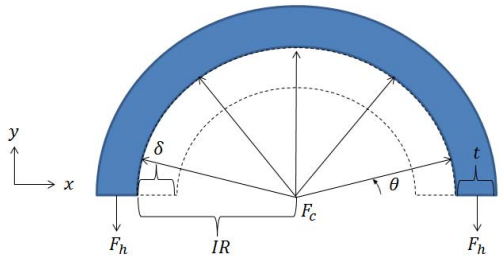

Fig. 2. Half of rotor cross section showing forces on carbon fiber retaining ring.

rotor under gravity. Analytical expressions are first derived for efficient preliminary design of the structure. These are followed by detailed finite-element analysis (FEA) to validate the analytical models.

A. Radial Expansion and Retaining Ring Hoop Stress

Since the proposed motor is a radial flux inside out design, the radial expansion will increase the airgap, which in turn increases air-gap reluctance in the motor magnetic circuit. To ensure motor electromagnetic performance and high power density, it is necessary to understand the tradeoffs between the key design parameters in the rotor structure.

Fig. 2 shows that force and stress in the retaining ring occurs mainly in the hoop direction. Force increases as speed increases, which causes elongation in the hoop direction. Hoop expansion causes an increased circumference which is directly proportional to diameter. Thus radial expansion is minimized when hoop elongation is minimized.

The hoop stress in the retaining ring is a result of the centrifugal force provided by the components beneath the ring spinning at high speeds. This is illustrated in Fig. 2, which shows the upper half of a circular cross section. The solid area is the retaining ring; the area enclosed by dashed-lines is the rest of the rotor components, which includes magnet segments and rotor shell. By considering the force balance of the free body diagram of the retaining ring the sum of forces in the vertical direction must be zero.

The hoop force can be obtained by integrating the centrifugal force over 180°, which equals twice the hoop force in the ring

$$F_h = \frac{v_{\mathrm{IR}}^2}{\mathrm{IR}}\left(\rho L \frac{\mathrm{IR}^2 - (\mathrm{IR}-\delta)^2}{2}\right) \tag{1}$$

where v_{IR} is the linear speed of the inner radius of the rotor, IR is the rotor inner radius, ρ is the average density of the titanium and magnets beneath the retaining ring, L is the axial length, and δ is the average depth of the pieces beneath the retaining ring.

The hoop stress is calculated by dividing the hoop force by retaining the ring cross-sectional area. Hooke's law is used to obtain the ring extension Δl and the radial expansion Δr. Note that the weight of the ring itself is neglected, for a first approximation, due to the relatively low density of the carbon fiber

$$\Delta r = \frac{\Delta l}{2\pi} = \frac{v_{\mathrm{IR}}^2 \rho}{2tE}(\mathrm{IR}^2 - (\mathrm{IR}-\delta)^2). \tag{2}$$

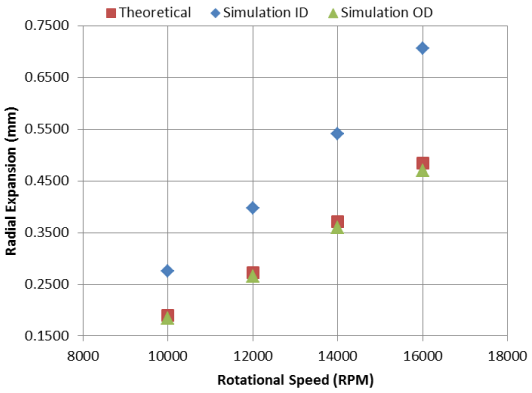

Fig. 3. Graphical comparison of rotor radial expansion calculation and simulation results with proposed retaining ring thickness and varied rotational speed.

TABLE II
ROTOR RADIAL EXPANSION CALCULATION AND SIMULATION RESULTS WITH PROPOSED RETAINING RING THICKNESS AND VARIED ROTATIONAL SPEED

RPM	Expansion (mm)		
	theoretical @ IR	Simulation @ ID	Simulation @ OD
10000	0.189	0.276	0.184
12000	0.272	0.396	0.265
14000	0.371	0.540	0.360
16000	0.484	0.706	0.471

The analytical prediction of the rotor expansion is compared with the results from an FEA simulation in Table II and Fig. 3. All FEA simulations were performed using "ANSYS Static Structural". A "fine" mesh was used for all simulations. A rotor retaining ring thickness of 0.5 in is used for calculations and simulations. In the simulations, the magnets and resin holding the magnets are modeled as a composite cylinder with an equivalent Young's Modulus to reduce computation time. The glue and magnets do not act as a structural member in the full machine. Thus using the composite structure is reasonable when evaluating radial expansion.

As shown in Fig. 3, the theoretical calculation closely approximates the simulated radial expansions at the outer diameter of the rotor. One explanation for the difference between the theoretical radial expansion and the inner diameter expansion in the simulation is the effect of Poisson's ratio, with the rotor components becoming radially thinner as the ring expands.

It can be observed that both the calculated results and the simulation results at rotor OD have second-order polynomial trend lines, indicating that the radial expansion is growing with the square of the rotor rotational speed. Similarly, the effect of rotor retaining ring thickness can also be investigated using (2). Equation (2) shows that the rotor radial expansion is proportional to the inverse of retaining ring thickness. The calculations and the FEA simulation results, at the rated speed of 14 000 rpm are compared in Table III and Fig. 4.

Unlike the speed variation cases, it can also be observed that the errors between the calculation results and the simulation

TABLE III
ROTOR RADIAL EXPANSION CALCULATION AND SIMULATION RESULTS WITH VARIED RETAINING RING THICKNESS AT 14 000 rpm

Retaining ring thickness (mm)	Radial Expansion (mm)		
	Theoretical	Simulation @ ID	Simulation @ OD
6.35	0.695	0.705	0.508
12.7	0.371	0.540	0.360
19.05	0.232	0.468	0.291
25.4	0.174	0.433	0.252

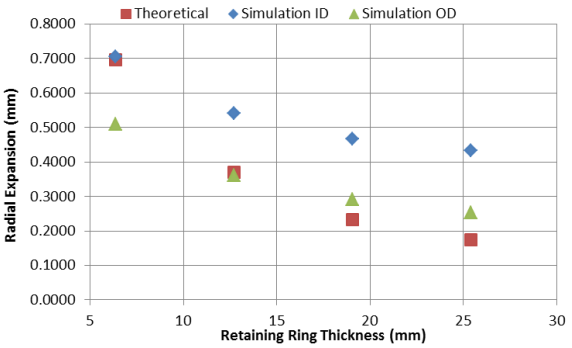

Fig. 4. Graphical comparison of rotor radial expansion calculation and simulation results with varied retaining ring thickness at 14 000 rpm.

results at rotor OD are not biased in a single direction. Even though from (2), it seems that the expansion is proportional to only the inverse of the retaining ring thickness, this is not accurate because the actual hoop force in the ring is also a function of thickness. The weight increase of the ring itself will increase the total centrifugal force. This fact is not captured in (1), where the hoop force is the result of the centrifugal force of components below the ring only. The retaining ring thickness of 0.5 in was found as a fair tradeoff between decreased expansion and reduction in weight, and is used in the final design.

Another method of reducing radial expansion is by increasing the Young's modulus of the retaining ring. However, since the Young's modulus of the chosen IM-7/PEEK carbon fiber composite is already high, 172.4 GPa, there are few other choices for retaining ring material which could combine both higher modulus and high strength-to-weight ratio.

The last parameter in (2) to reduce expansion is the diameter of the retaining ring. The electromagnetics have been optimized with the mechanical design through an iterative process. Since the magnetic loading and the electric loading have been optimized, changing diameter is not a straightforward method of reducing expansion while retaining power density.

It must be noted that the expansion of the rotor was included in a combined electromagnetic and mechanical-coupled analysis. This analysis occurred to find the effect of rotor expansion on the torque produced by the machine. Due to the toothless geometry of the machine, the magnetic airgap includes not only the mechanical airgap but also the copper winding area. Because the magnetic airgap is so large, the increase of the mechanical airgap has a relatively small effect on the torque produced.

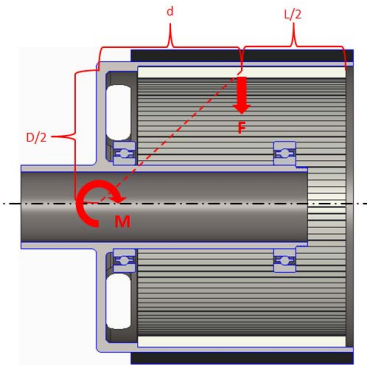

Fig. 5. Equivalent moment relation diagram.

B. Bending

The external rotor with cantilevered support from one end also introduces another structural challenge, bending due to gravity when the motor is mounted horizontally. This can be mitigated by mounting the rotor vertically, but this is likely not an option for an electric aircraft. Fig. 5 shows the cross-sectional view of the motor, where the active region of the rotor is supported by an end plate at the drive end. The rotor will deform even while not rotating, as the free end will sag in the direction of gravity. Through FEA it was determined that bending occurs mainly through the rotor end plate. This may be modeled as a bending moment, calculated using the following equation:

$$M = Fd = m_{\text{tran}} g d \tag{3}$$

where F is the equivalent force as a result of the weight of transverse section, m_{tran} is the mass of transverse section, and d is the distance of equivalent force to end plate center.

The deformation of end plate is analogous to a cantilevered beam bending deformation. To understand what parameters determine the bending deformation, the maximum deflection of a cantilever beam is used [5]

$$\delta_{\max} = \frac{f l^3}{3\text{EI}}. \tag{4}$$

The force f in the above beam bending equation is proportional to the weight of the rotor transverse section. Also, the beam length l in the equation has a linear relationship with the plate diameter. Even though the I in equation is the area moment of inertia of a beam with constant cross section, it is still informative if it is compared with the cross section of the end plate, with D being the plate diameter, and t being the plate thickness. For the end plate bending direction shown in Fig. 5, the area moment of inertia for this cross section is obtained in [6].

After substituting the expected force on end of the beam, the mass of the transverse portion, along with other geometric parameters into (4), the following relationship was found:

$$\delta_{\max} \propto \frac{\text{FL}^3}{3\text{EI}} = \frac{\frac{m_{\text{tran}} g}{2}\left(\frac{D}{2}\right)^3}{3E\frac{Dt^3}{12}} \propto \frac{m_{\text{tran}} g D^2}{Et^3}. \tag{5}$$

From (5), it can be observed that increasing the end plate thickness is an effective approach to reducing the static deflection because the deflection is inversely proportional to the

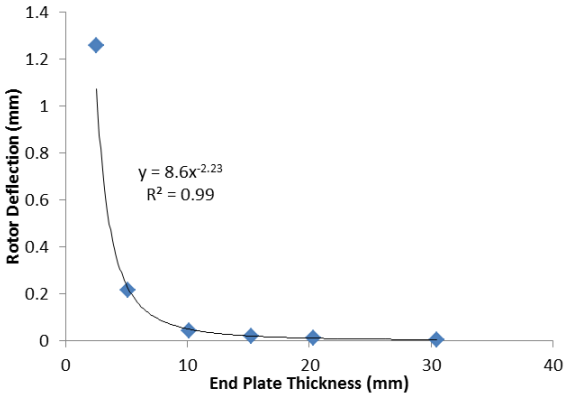

Fig. 6. Data trend line for rotor deflection with different end plate thickness.

cube of end plate thickness. To confirm this theory, structural FEAs were performed for designs with different end plate thicknesses, as shown in Fig. 6.

For a specific motor design, a quantitative numerical relationship between rotor static deflection and key geometric parameters is still achievable using the FEA trial method. For the proposed design, in this paper, the relationship between static deflection and end plate thickness is obtained from the data trend line of the FEA results, both in units of millimetre, as shown in Fig. 6.

The optimal end plate thickness should be chosen as the point near the knee of the curve in Fig. 6, because it effectively restrained the rotor static deflection without using excessive materials. The chosen rotor end plate thickness for the proposed motor design is 10.2 mm.

Other approaches to reduce the rotor static deflection can also be observed from (5), such as using material with higher elastic modulus for the rotor shell, reducing the mass of the rotor transverse section, and reducing the rotor diameter. Stiffeners, such as ribs were not used due to manufacturing challenges and space constraints.

III. Design for Dynamics

During dynamic operation of an electric machine, there are various vibrations caused by rotational or electromagnetic forces with different force shapes, frequencies, and amplitudes. In addition, everything has at least one resonant frequency. When these vibrations intersect, it can cause fatigue failure which decreases lifetime, sometimes to sudden failure [7]. This is especially true for the thin radial builds of the proposed motor, because unlike normal electric motors, it does not have a thick steel back yoke to dampen vibration and reduce stress. This section deals with the two major components of vibration analysis, static and rotating.

A. Stator Resonance Mode

Stationary vibration analysis focuses on designing the stator structure so that vibration source frequencies and resonant frequencies do not intersect, while paying attention to motor power density. First, vibrational sources are explored. Second, the resonant modes are found. Finally, the interaction of these modes is explored.

TABLE IV
Stator Resonance Modes Obtained by FEA Simulations

Mode	Frequency (Hz)	Shape
2	1363.6	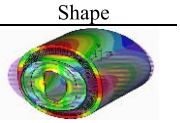
3	2150	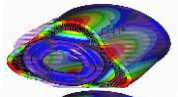
4	2929.4	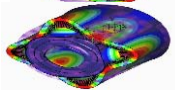
5	3916.9	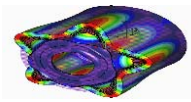
6	5105.3	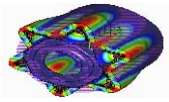
10	11352	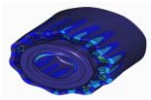

The possible sources of cyclic force in the stator that result in vibration are explored in [7], [8], and [9]. For stator vibration, there are four important sources. The first is cyclic forces at twice the frequency of the motor electrical power supply. Since the motor electrical frequency is the same as the frequency of its rotating air-gap flux, the cyclic magnetic pull force will always be present in an electric machine at twice the electric frequency. This frequency occurs in the airgap, and is a cylindrical sinusoidal force. The second is the rotational frequency, where any mechanical modes will be excited. This frequency is caused by a rotational force. The third is the "tooth" harmonics, eliminated in this machine due to our toothless design. Through the use of Halbach arrays, the flux density in the airgap minimizes space harmonics, which is a fourth source of vibrations. Thus, though four sources exist, two have been eliminated through design.

After obtaining the excitation frequencies of potential sources of cyclic force, the second step is to investigate resonance modes. For a given stator geometry, resonant mode shapes and frequencies can be calculated numerically. Both steps are necessary to determine whether the designed motor will experience resonant vibration. Resonant vibration only occurs when both the frequency of the cyclic force is at or near a resonant frequency and the cyclic force has a shape to deform the structure to the particular mode shape of that resonant frequency. Examples of mode shapes found through FEA and their corresponding frequencies may be found in Table IV.

The modes shapes were obtained through an FEA analysis of the stator with the geometry in Fig. 7. The analysis was designed to find all the resonance modes of the structure up to a frequency of 20 000 Hz. However, only the mode shapes with radial nodes patterns were summarized in Table IV. Other mode shapes, such as those with warping deformation along the axial length or with torsional deformation, were not shown

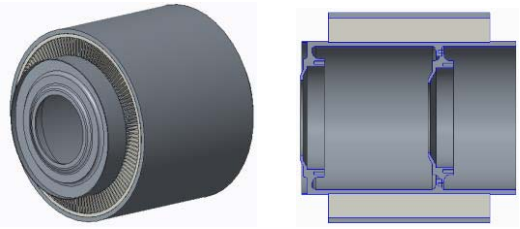

Fig. 7. Stator for modal analysis, isometric view (left) and section view (right).

here, because they could not be excited by the sources of cyclic force. In the results, the mode index number corresponds to the number of nodes of the radial patterns.

For machine design, the resonant modes of a structure are usually obtained through an FEA modal analysis. However, for the purpose of interdisciplinary optimization, it is necessary to analytically express the resonant frequency of a given mode shape, so that the tradeoffs between design parameters can be used to achieve the ultimate goal of a high power density motor design. This analytical model is obtained in a method similar to that presented in [7], in which the motor is essentially "unrolled" into a beam.

After approximating the unrolled beam structure as a simply supported beam with a fixed–fixed end condition, the natural frequency of the stator can be calculated using the equation for the fundamental frequency of a beam [10]. By using results from both [7] and [10], the resonant frequency of the stator for a selected mode shape can be analytically obtained as follows:

$$f = \frac{2M^2}{\pi^3}\left(\frac{22.373}{D^2}\right)\sqrt{\frac{\mathrm{EI}}{\rho}} \tag{6}$$

where E is the material elastic modulus, I is the area moment of inertia of the beam cross section, ρ is the linear density of the stator, and D is the length of the beam. It was observed that both the simulation results and the theoretical calculations have second-order polynomial trend lines. There are discrepancies between the analytical and FEA analysis, so any design must be validated by FEA. These discrepancies come from the over-simplified approximation of the complicated stator structure using a simple beam model.

To address concerns about resonant vibrations, it is necessary to determine whether the sources of cyclic force in the motor will coincide with structural resonance modes. The vibrations at the fundamental rotor rotational frequency can quickly be excluded from the risks of resonance vibration due to the low frequency. For the proposed design, the highest speed of normal operation is 14 000 rpm, which gives a frequency of 233.33 Hz. The frequency of the lowest resonance mode, the two-node mode, from either the theoretical calculation (709 Hz) or the FEA simulation (1364 Hz) is much higher than the rotor rotational frequency.

The main concern is the vibration source at twice the line frequency. This is the electromagnetic force experienced by the stator every time a pole passes by. This excitation force has a frequency of 4667 Hz, which is relatively high compared with that of the normal four-pole or eight-pole motors with lower operational speed. However, even though the frequency

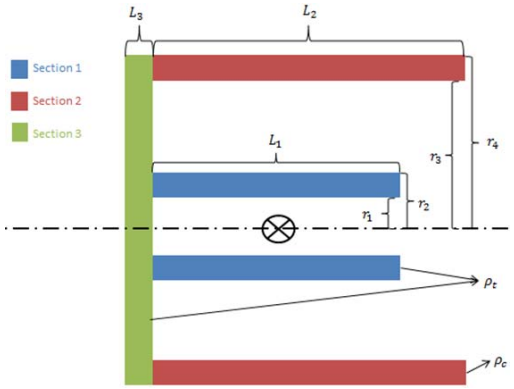

Fig. 8. Cross section of the simplified rotor structure.

of this electromagnetic excitation force increases with the number of motor poles, the risk of resonant vibration does not necessarily increase. The resonance mode shape for a 20-pole motor should have radial pattern of 20 nodes. As can be seen in Table IV, the resonance mode with the 10-nodes pattern already has a resonant frequency of about 11 352 Hz, well above that of the twice electrical frequency. The expected resonant frequency for the 20-nodes mode, which is about 36 256 Hz, will be much higher than the pole passing frequency.

It is reasonable to suspect potential vibration that can excite resonance modes with the integer factor of 20-nodes, which in this case are 2-, 4-, 5-, and 10-node modes. Among them, only the 2-, 4-, and 5-node modes fall below the rated 4667 Hz twice line frequency. This is a concern as these modes could be excited during ramp up and down from the rated speed. Thus, the twice electrical frequency should not dwell at the modal frequencies corresponding to the 2-, 4-, and 5-node modes. This can be achieved by ramping up the machine quickly.

B. Rotordynamics

Similar to concerns for instability in the stator during dynamic operation, the rotor is also subject to vibration issues. The rotordynamics are especially important due to the high operating and tip speeds. First, analytical relationships are found to understand the relationships between the key parameters of the system. Second, a numerical FEA is used for the detailed design of bearing stiffness and for full analysis of the rotordynamics.

In order to do analytical analysis, the complex nonlinear models of rotordynamic systems are frequently simplified. Common simplification methods include consideration of a symmetrical rigid rotor [12] or a Jeffcott rotor [13]. The simplification used in this section will follow [11], where detailed derivations were done while considering the gyroscopic effect. The analytical expressions below will demonstrate the dependence of modal frequencies of the system on the geometry and rotating speed. Also, the gyroscopic effect can increase or decrease the modal frequencies, as a function of the rotor speed.

The proposed rotor design can be considered as the simplified geometry, as shown in Fig. 8. Section I is the rotor shaft

on which the bearings sit. Section II consists of three layers of materials—the carbon fiber retaining ring, titanium rotor shell, and the magnets. Section III is the rotor end plate, which is a cylindrical structure. The material densities of both Section I and Section III are the density of titanium ρ_t. The density of Section II is the composite density with the weighted average of the three materials densities ρ_c. Therefore, the polar moment of inertia and the transverse moment of inertia of the rotor structure can be calculated using the parallel axis theorem by adding the moment of inertia of each section.

For polar moment of inertia, since the three sections are rotating about the same axis, the total polar moment of inertia of the rotor is simply the sum of all sections about their center of mass. The polar moment of inertia for Sections I and II can be calculated as hollow cylinders and for Section III as a solid cylinder. The moment of inertia equations for the two sections about their center of mass are presented in [14].

As for transverse moment of inertia, since the bearings are sitting on both ends of Section I, the transverse moment of inertia of the whole rotor is calculated about the axis perpendicular to paper at the $(L_1/2)$ location of Section I. Therefore, the parallel axis theorem is applied for Sections II and III. The total transverse moment of inertia is calculated similarly using [14].

An important characteristic of the rotor in this section is the ratio of the polar to the transverse moment of inertia, P. Generally, this ratio will be large if the rotor has large diameter but short axially. If the rotor is designed to be small in diameter but long in axially, the ratio will be small and closer to zero. It is crucial that this ratio be outside of the 0.8 to 1.2 range [15]. The proposed design has a ratio about 1.2. Since the ratio is greater than unity, the gyroscopic effect will contribute apparent stiffness to the rotor system. This raises forward whirling mode frequencies [16].

The dynamics of a rotating system is actually the interaction between the rotor inertial force and the stiffness/damping forces generated by the lateral deformation of the shaft. This is expressed in the equations of motion of the system [11]. For simplification, both bearings are assumed to have the same stiffness, and the center of mass of the whole rotor is assumed to be in the middle of Section I. Thus, the solution to the characteristic equations of the above differential equation will have similar forms as presented in [11].

The cylindrical mode natural frequency, corresponding to the rotor translational or parallel motion, is found to be

$$\omega_n = \pm\sqrt{\frac{2k}{m}} \tag{7}$$

where k is the radial stiffness of the bearing and m is the mass of the rotor.

The conical mode natural frequency is obtained from the solution of the characteristic equations corresponding to the angular dynamics of the rotor. These dynamics include the effect of gyroscopic moment acting on the rotor, which will affect the mode natural frequency as a function of rotor speed. In order to find these rotating frequencies, the conical mode natural frequency is obtained for a stationary rotor. This is shown below where I_{tot} is the transverse moment of inertia

$$\omega_{n0} = \sqrt{\frac{kL_1^2}{2I_{\text{tot}}}} \tag{8}$$

when the rotor is rotating, the conical mode natural frequency is shown as below. The plus and minus signs correspond to the forward and backward modes, respectively, and ω is the rotational speed

$$\omega_n = -\frac{P\omega}{2} \pm \sqrt{\left(\frac{P\omega}{2}\right)^2 + \omega_{n0}^2}. \tag{9}$$

First, from (7)–(9), it can be observed that by increasing the stiffness of the system, the resonance mode frequency can be increased. For both cylindrical mode and conical mode, the natural frequency is proportional to the square root of the bearing stiffness. The bearing stiffness is proportional to a factor of the applied preload, which in turn is generally proportional to the size of the bearing and its type. In general, there is a tradeoff between the size or stiffness of bearing and the rotational speed. As the size increases, and thus the stiffness, the rotational speed decreases. Thus, for the rotor design, bearings should be chosen first with a rated speed higher than the rotor-rated speed and with enough stiffness to raise the natural frequencies out of dangerous levels.

To analyze the bearings with more fidelity an FEA solver using 1-D beam elements, XLRotor, is used. Four modes were observed below 50 000 cpm, three conical and one cylindrical. The bearing stiffness, k was varied, and the following natural frequency map at 14 000 rpm was found (Fig. 9).

The results indicate that by increasing the bearing radial stiffness, the natural frequencies of all resonant modes increase. It is also observed that the natural frequencies of modes 2 and 3 are sensitive to the change of bearing stiffness at low values, as the curves are steep in the beginning, but flatten out later. Since mode 3 is close to a cylindrical mode, its trend line has a power close to 0.5, which coincides with (7). Using a power-type trend line for other modes does not give good approximations. This is expected because, after plugging (8) into (9), the natural frequency of the nonzero speeds conical mode is not proportional to the square root of bearing stiffness for conical modes.

From (8) and (9), it can also be observed that the structure moment of inertia plays a role in the natural frequency of conical modes. Equation (8) indicates that the natural frequency of zero-speed conical modes increases as the rotor transverse moment of inertia I_{tot} decreases. Equation (9) shows that the increase of the moment of inertia ratio P can increase the nonzero speed conical mode frequency. Therefore, in order to increase the conical mode natural frequency, the rotor polar to transverse moment of inertia ratio needs to increase. Thus rotordynamics improve with a larger diameter and shorter axial length. However, this conclusion is counter-intuitive when considering the design to maximize stator resonant frequencies away from forcing frequencies, because (6) implies that smaller diameter designs can increase the resonant frequencies for stator modes with radial patterns. Therefore, the selected

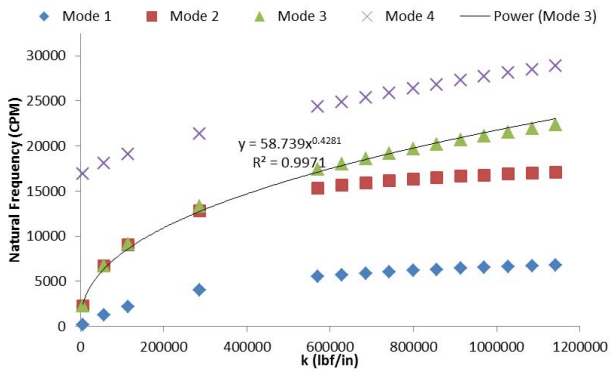

Fig. 9. Rotor natural frequencies at different bearing system stiffness.

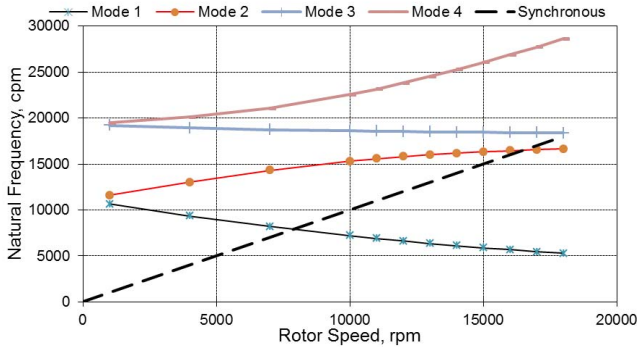

Fig. 10. Campbell diagram of rotor-dynamic system in the proposed design.

design balances the tradeoff between the stator resonant vibration performance and the rotordynamic performance.

The Campbell diagram generated by XLRotor is shown in Fig. 10. For speed ramp-up to the rated speed of 14 000 rpm, the designed rotor will only encounter one vibration mode, mode 1. Since mode 1 is a backward whirling mode, indicated by its natural frequency decreasing as rotor speed increases, it will not cause serious vibration problems as long as the motor moves past that speed without staying near that speed. Also most high performance machines operate above their first resonance mode [11]. The rotor will not encounter the next mode, until a speed of 16 500 rpm. Thus, it has a speed margin, the margin between the forcing frequency and the modal frequency, greater than 15%, a common practice in industrial applications [11].

IV. Experimental Results

A full size prototype rotor has been built to demonstrate the soundness of the design and to validate the analysis methods presented in this paper. The testing occurred at Test Devices Inc. The displacement of the rotor was measured through the use of proximity probes placed where the stator typically resides. The test setup is shown in Fig. 11.

First, a proof test was performed up to the rated speed of 15 000 rpm. This proof test confirmed that the rotor will not fly apart at speed. Expansion results were then obtained, and are shown in Fig. 12. The maximum theoretical expansion closely

Fig. 11. Test setup.

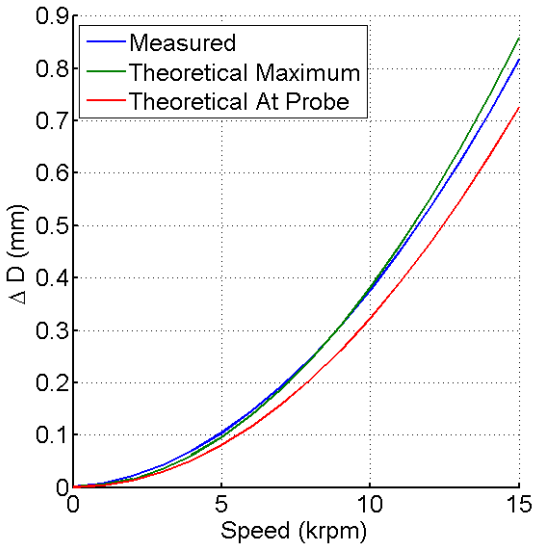

Fig. 12. Expansion results.

correlates with the measured expansion. However, at the probe, the difference in expansion is as great as 12.3%. This is likely due to not fully capturing the properties of either the carbon fiber or glue. This will be taken into account in building the full machine.

Another XLRotor file has been created based on the experimental setup shown above. The test setup results indicate that there could be critical frequencies at 150, 1200, 2300, and 12 880 rpm. These results are very different from those shown in Fig. 10. Though these results are different, a verification of the test rotordynamic model can be taken as a verification of the machine rotordynamic model.

The vibration data of the rotor was captured for the proof test. This occurred through a proximity probe mounted near

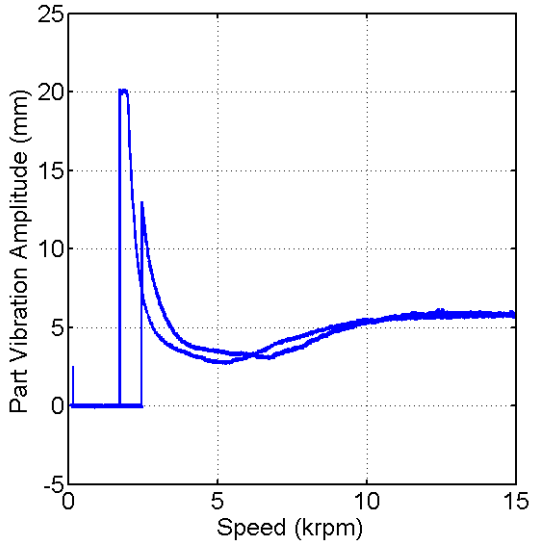

Fig. 13. Rotordynamics results.

the top of the rotor. The results of this test may be found in Fig. 13. The amplitude of vibration is plotted as the rotor-ramped up and down. Through looking at the amplitude as the rotor speed increases, the natural frequencies are excited at 2000 and 12 500 rpm. The 12 500-rpm frequency does not affect the amplitude very much, but is present. The percent error between these measured frequencies and the expected natural frequency is 13% and 3% for the top two theoretical frequencies, respectively. This error is likely due to the 3-D nature of the fan and associated holes, which are difficult to analyze in XLRotor. These results are reasonable for frequency spectrum analysis and corroborate the analyses done previously.

V. Conclusion

The proposed motor design with rated output power of 1 MW and rated speed of 14 000 RPM has potential to reach a power density as high as 14.4 kW/kg. To maximize motor power density, the motor needs to have a structure that will efficiently use materials to provide a structurally sound design. A permanent magnet-type motor with an inside out configuration was chosen because of the advantages of high peak efficiency and potential power density compared to other motor types. Because, until now there are relatively few mature motor designs using the inside out configuration for such high power level applications, the mechanical design of the proposed motor needs to be studied in a cross-functional manner. Since the motor weight reduction was important in this research, the effect of structural parameters to the motor mechanical performance was studied here.

The high rotor rotational speeds and unconventional inside out configuration cause motor structural deformation at steady-state operation and introduce challenges for motor structural design to achieve desired performance. Major challenges include the rotor radial expansion due to the centrifugal effect of a rotating rotor and the rotor static deflection due to the effect of gravity, both of which are optimized for least amount of deformation.

The proposed motor design was also subject to vibrational issues during dynamic operation. These challenges are due to high-frequency harmonics present in the motor and the relatively thin radial builds compared to ground application machines. The motor vibration was analyzed in the two main components independently. The vibration analysis for stationary components emphasized the stator resonance modes. For rotor system dynamics, the mode frequency could be increased with the system stiffness.

This paper shows that designing high-specific-power electric machines causes mechanical challenges due to the low weight and high speed. These structural deformation challenges, radial expansion and bending were analyzed and radial expansion are experimentally validated. The vibrational issues for both stator and rotor were analyzed and a rotordynamic model was validated. This paper shows that through fully understanding the mechanical issues, they can be mitigated through appropriate material and dimensional selection and tradeoffs. Future work includes a rotodynamic setup which utilizes the specified bearing system, stator experimental validation, and full machine validation.

References

[1] R. DelRosario, "A future with hybrid electric propulsion systems: A NASA perspective," in *Proc. Turbine Eng. Technol. Symp.*, Sep. 2014.
[2] A. Yoon, X. Yi, J. Martin, Y. Chen, and K. Haran, "A high-speed, high-frequency, air-core PM machine for aircraft application," in *Proc. IEEE Power Energy Conf. Illinois (PECI)*, Feb. 2016, pp. 1–4.
[3] X. Zhang and K. S. Haran, "High-specific-power electric machines for electrified transportation applications-technology options," in *Proc. IEEE ECCE*, Sep. 2016, pp. 1–8.
[4] J. Martin, A. Yoon, and K. Haran, "Design of high-frequency Litz 'air-gap' windings for high-power density electrical machines," in *Proc. EMCW Conf.*, 2016, pp. 798–805.
[5] *Beam Design Formulas With Shear and Moment Diagrams*, document Design Aid 6, American Forest and Paper Association, Jun. 2016.
[6] The Engineering Toolbox. *Area Moment of Inertia*. Accessed on Jun. 2016. [Online]. Available: http://www.engineeringtoolbox.com/area-moment-inertia-d_132.html
[7] W. R. Finley, M. M. Hodowanec, and W. G. Holter, "An analytical approach to solving motor vibration problems," *IEEE Trans. Ind. Appl.*, vol. 36, no. 5, pp. 1467–1480, Sep./Oct. 2000.
[8] W. Tong, "Motor vibration and acoustic noise," in *Mechanical Design of Electric Motors*, vol. 28. Boca Raton, FL, USA: CRC Press, Apr. 2014, pp. 481–549.
[9] G. H. Bate, "Vibration diagnostics for industrial electric motor drives," Brüel Kjær, Nærum, Denmark, Appl. Note, 1987.
[10] T. Irvine. (Nov. 2012). *Bending Frequencies of Beams, Rods, and Pipes Revision S*. [Online]. Available: http://www.vibrationdata.com/tutorials2/beam.pdf
[11] S. Y. Yoon, Z. Lin, and P. E. Allaire, "Introduction to rotor dynamics," in *Control of Surge in Centrifugal Compressors by Active Magnetic Bearings*. London, U.K.: Springer, 2013, pp. 17–55.
[12] T.-N. Shiau and A.-N. Jean, "Prediction of periodic response of flexible mechanical systems with nonlinear characteristics," *J. Vibrat. Acoust.*, vol. 112, no. 4, pp. 501–507, 1990.
[13] Y. B. Kim and S. T. Noah, "Response and bifurcation analysis of a MDOF rotor system with a strong nonlinearity," *Nonlinear Dyn.*, vol. 2, no. 3, pp. 215–234, 1991.
[14] R. A. Serway and J. W. Jewett, *Physics for Scientists and Engineers With Modern Physics*, 9th ed. Boston, MA, USA: Cengage Learning, 2013.
[15] R. H. Jansen and T. P. Dever, "G2 flywheel module design," NASA, Washington, DC, USA, Tech. Note CR-2006-213862, Aug. 2006, pp. 1–20.
[16] W. D. Marscher, "An end-user's guide to centrifugal pump rotordynamics," in *Proc. 23rd Pump Users Symp.*, 2007, pp. 69–84.

Yuanshan Chen (M'15) received the bachelor's degree in mechanical engineering and the master's degree in electrical and computer engineering from the University of Illinois at Urbana-Champaign, Champaign, IL, USA.

He was a Research Assistant of the NASA Fixed Wing Project for a high power density electric motor.

Reed Sanchez (M'15) is currently with Dr. Haran's group at the University of Illinois with a background in mechanical engineering, Colorado School of Mines, Golden, CO, USA. His experience and education in both mechanical and electrical engineering contributes a multidimensional understanding of both sides of these machines to his research.

Andy Yoon (S'14) received the bachelor's and master's degrees in electrical and computer engineering from the University of Illinois at Urbana-Champaign, Champaign, IL, USA, in 2013 and 2016.

He is currently working with a Prof. K. Haran at the University of Illinois at Urbana-Champaign.

Kiruba Sivasubramaniam Haran (F'00) received the B.S. degree in electrical engineering from Obafemi Awolowo University, Ife, Nigeria, in 1994, and the Ph.D. degree in electric power engineering from the Rensselaer Polytechnic Institute, Troy, NY, USA, in 2000.

He was at GEGE Research Center in Niskayuna, NY, USA, for 13 years, and led the research group that develops advanced electrical machine technology for all of GE's industrial businesses. He is currently an Associate Professor of electrical engineering with the University of Illinois at Urbana-Champaign, Champaign, IL, USA.